crystals

MDPI

Communication

Topological Valley Transport of Elastic Waves Based on Periodic Triangular-Lattices

Zehuan Tang [1], Jiachao Xu [1], Bowei Wu [1], Shuanghuizhi Li [1,*], Fei Sun [1], Tingfeng Ma [1], Iren Kuznetsova [2], Ilya Nedospasov [2], Boyue Su [1] and Pengfei Kang [1]

[1] School of Mechanical Engineering and Mechanics, Ningbo University, Ningbo 315211, China
[2] Institute of Radio Engineering and Electronics of RAS, 125009 Moscow, Russia
[*] Correspondence: 2111081008@nbu.edu.cn; Tel.: +86-15-207-422-135

Abstract: Topological transports of elastic waves have attracted much attention because of their unique immunity to defects and backscattering-suppression ability. Periodic lattice structures are ideal carriers of elastic-wave transports due to their ability to manipulate elastic waves. Compared with honeycomb-lattice structures, the wave-guide-path designs of triangular-lattice structures have higher flexibility. In this paper, topological transports of elastic waves in the periodic triangular-lattice structure are explored. It is shown that differences between intra-coupling and inter-coupling radii can cause the destruction of the effective spatial inversion symmetry, which gives rise to the valley Hall phase transition and the forming of topological edge states. Utilizing valley Hall effect, topological transports of elastic waves traveling along linear and Z-shaped waveguides are realized with low scattering and immunity to defects. On this basis, the path-selection function of transports of elastic waves in periodic triangular-lattice structures is obtained. Topological valley Hall edge states of elastic waves in periodic triangular-lattice structures have a good application prospects in elastic-wave manipulations and communications.

Keywords: topological edge states; valley Hall effect; periodic triangular lattice; elastic waves

check for updates

Citation: Tang, Z.; Xu, J.; Wu, B.; Li, S.; Sun, F.; Ma, T.; Kuznetsova, I.; Nedospasov, I.; Su, B.; Kang, P. Topological Valley Transport of Elastic Waves Based on Periodic Triangular-Lattices. *Crystals* **2023**, *13*, 67. https://doi.org/10.3390/cryst13010067

Academic Editors: Kuo-Chih Chuang, Yanfeng Wang, Yongquan Liu and Yuri Kivshar

Received: 21 November 2022
Revised: 18 December 2022
Accepted: 28 December 2022
Published: 30 December 2022

1. Introduction

Acoustic waves can carry out logical operation, signal processing, and accurate measurement of multiple physical parameters [1–7]. These advantages of acoustic waves are particularly prominent in solids, which propagate in the form of elastic waves. In recent years, as a carrier of information and energy, elastic waves have become a hot spot of concern, which have several important advantages, such as strong anti-interference ability [8], low transmission loss [9,10], and large information capacity [11]. In addition, elastic-wave devices are easy to integrate, and are thus widely used in traditional fields such as wireless communication, passive sensing, nondestructive testing, geological exploration, as well as the rapidly quantum computing, and so on. However, there are still many problems in elastic wave transports [12,13]; for instance, the existence of too much scattering can cause problems and the transport effect is sensitive to defects in the structure.

Topological protections provide unprecedented opportunities for wave manipulation and energy transport in various physical fields [14,15], including elasticity, acoustics, quantum mechanics, and electromagnetisms. Elastic waves with topological protections can achieve lossless transport through suppressing backscattering and are immune to various defects and impurities [13,16,17]. There is no wave propagation inside the topological insulator. On the interface composed of two kinds of topological insulators with different phases or the boundary of the topological insulator itself, the wave energy can be transported with topological protections. Lattice structures have a wide application prospect in topological insulators because the propagation of elastic waves in this type of structure are easily controlled [18]. Previously, lattice-structure based topological transports were realized mainly on honeycomb-lattice [19] and kagome-lattice structures [20,21], for which, the construction of the path lacks flexibility. The periodic triangular-lattice structure has a good application prospect in topological transport of elastic waves due to its simplicity in structure. The structure has uniform mass-point arrangement and all mass-points are distributed on straight lines, thus straight and bend wave-guide paths can both realized easily, namely the wave-guide-path designs have higher flexibility.

In this work, by breaking the spatial symmetry of the structure by changing the intra-coupling and inter-coupling radii, a valley Hall topological insulator based on periodic triangular-lattices is constructed to realize topological transports of elastic waves, and its immunities to defects and path corners are verified. On this basis, a direction-selective elastic energy splitter based on periodic triangular-lattice structures is designed.

2. Model

The triangular-lattice structure is shown in Figure 1a, where a is the lattice constant and $\vec{a_1}$ and $\vec{a_2}$ are lattice vectors. The unit cell of the triangular lattice is represented within the dashed frame in Figure 1a and a zoomed-in figure is shown in Figure 1b. The inter-coupling and intra-coupling radii between cylinders, namely radii of round bars responsible for intra-coupling and inter-coupling of the unit cell, are set as R_1 and R_2, respectively. The cylinder radii are both R, and the cylinder height is h_d. The parameters are set as: $R = 5$ mm, $R_1 = 3$mm, $R_2 = 0.8$ mm, $h_d = 15$ mm.

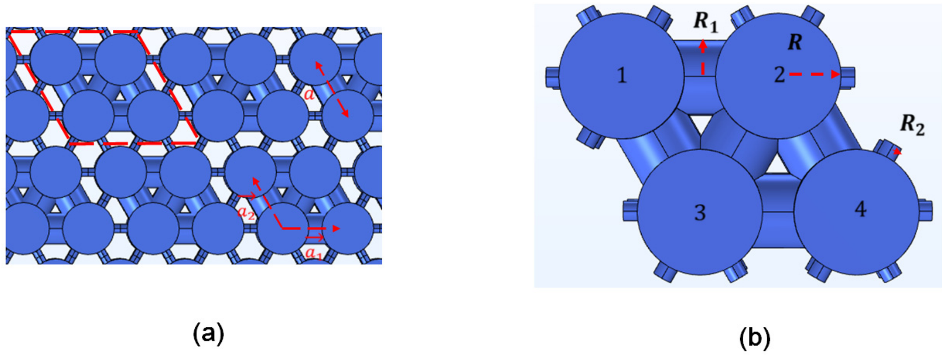

Figure 1. (**a**) Schematic diagram of periodic triangular-lattice structure; (**b**) Unit cell.

Assuming a time dependence of the form $e^{-i\omega t}$, the time independent elastic wave equation in a homogeneous medium [22] can be written as

$$(\lambda + 2\mu)\nabla(\nabla \cdot \mathbf{u}) - \mu\nabla \times \nabla \times \mathbf{u} + \rho\omega^2\mathbf{u} = 0, \quad (1)$$

where $\mathbf{u}$ is the displacement vector, and ρ is the mass density. λ, μ are Lame coefficients of the medium, which are related to Young's modulus and Poisson's ratio. This equation gives rise to uncoupled longitudinal and shear waves with velocities $c_l = \sqrt{(\lambda + 2\mu)/\rho}$ and $c_s = \sqrt{\mu/\rho}$, respectively. In the structure shown in Figure 1, by detuning the values of radii R_1 and R_2, the inter-couplings and intra-couplings of the unit cell change accordingly. Thus, the space-inversion symmetry can be broken, which gives rise to gapless edge states. In order to clearly explain the influence of inter-coupling and intra-coupling radii, the tight-binding model is used to describe this structure.

The governing equation of vibrations of the system can be written as:

$$\mathbf{M}\ddot{\mathbf{u}} + \mathbf{K}\mathbf{u} = \mathbf{P}(t), \quad (2)$$

where $\mathbf{M}$ represents mass matrix, $\ddot{\mathbf{u}}$ is acceleration matrix, $\mathbf{K}$ stands for stiffness matrix, $\mathbf{u}$ is displacement matrix, and $\mathbf{P}(t)$ stands for load matrix. In this case, the load matrix $\mathbf{P}(t) = 0$ is considered. Thus, the motion governing equation can be written as

$$\mathbf{M}\ddot{\mathbf{u}} + \mathbf{K}\mathbf{u} = 0, \quad (3)$$

The basis vector in three directions of the lattice of the unit cell satisfies:

$$\begin{aligned}
&|r_1| + |r_2| + |r_3| = 1, \\
&r_1 + r_2 + r_3 = 0, \\
&\langle r_1, r_2 \rangle = \langle r_2, r_3 \rangle = \langle r_3, r_1 \rangle = \tfrac{1}{2}.
\end{aligned} \tag{4}$$

The unit cell in Figure 1b contains four masses of value m, the radii of intra-bars and inter-bars are denoted by R_1 and R_2, respectively, corresponding to equivalent intra-coupling and inter-coupling spring constants k_1 and k_2, respectively. Letting $\mathbf{u}_j^{\mathbf{r}}$ be the displacement of mass j in the unit cell ($\mathbf{r}$), a Floquet–Bloch wave of wave number k and frequency ω is characterized by

$$\mathbf{u}_j^{\mathbf{r}} = \mathbf{u}_{\mathbf{k}}(j) e^{i(k\cdot\mathbf{r} - \omega t)} \tag{5}$$

By using the tight-binding model, according to Equation (3), the governing equations for the four cylinders in the unit cell are obtained, namely

$$\begin{aligned}
&-m\omega^2 u_1 = k_1 \langle u_2 - u_1, r_1 \rangle r_1 + k_2 \langle Q_1^* u_2 - u_1, r_1 \rangle r_1 \\
&+ k_1 \langle u_3 - u_1, r_2 \rangle r_2 + k_2 \langle Q_2 u_3 - u_1, r_2 \rangle r_2 \\
&+ k_2 \langle Q_3 u_4 - u_1, r_3 \rangle r_3 + k_2 \langle Q_3^* u_4 - u_1, r_3 \rangle r_3,
\end{aligned} \tag{6}$$

$$\begin{aligned}
&-m\omega^2 u_2 = k_1 \langle u_1 - u_2, r_1 \rangle r_1 + k_2 \langle Q_1 u_1 - u_2, r_1 \rangle r_1 \\
&+ k_1 \langle u_3 - u_2, r_3 \rangle r_3 + k_2 \langle Q_3^* u_3 - u_2, r_3 \rangle r_3 \\
&+ k_1 \langle u_4 - u_2, r_2 \rangle r_2 + k_2 \langle Q_2 u_4 - u_2, r_2 \rangle r_2,
\end{aligned} \tag{7}$$

$$\begin{aligned}
&-m\omega^2 u_3 = k_1 \langle u_1 - u_3, r_2 \rangle r_2 + k_2 \langle Q_2^* u_1 - u_3, r_2 \rangle r_2 \\
&+ k_1 \langle u_2 - u_3, r_3 \rangle r_3 + k_2 \langle Q_3 u_2 - u_3, r_3 \rangle r_3 \\
&+ k_1 \langle u_4 - u_3, r_1 \rangle r_1 + k_2 \langle Q_1^* u_4 - u_3, r_1 \rangle r_1,
\end{aligned} \tag{8}$$

$$\begin{aligned}
&-m\omega^2 u_4 = k_2 \langle Q_3 u_1 - u_4, r_3 \rangle r_3 + k_2 \langle Q_3^* u_1 - u_4, r_3 \rangle r_3 \\
&+ k_1 \langle u_2 - u_4, r_2 \rangle r_2 + k_2 \langle Q_2^* u_2 - u_4, r_2 \rangle r_2 \\
&+ k_1 \langle u_3 - u_4, r_1 \rangle r_1 + k_2 \langle Q_1 u_3 - u_4, r_1 \rangle r_1.
\end{aligned} \tag{9}$$

According to Bloch's theorem:

$$\begin{aligned}
Q_j^* &= e^{-iq_j}, \\
Q_j &= e^{iq_j},
\end{aligned} \tag{10}$$

where $q_j = \langle \mathbf{q}, \mathbf{r}_j \rangle$, for $j = 1, 2, 3$.

From Equations (6)–(9), it can be seen that intra-coupling radii R_1 and inter-coupling R_2 influence status of motions of four cylinders in the unit cell. Through change the relative size of R_1 and R_2, the effective spatial symmetry can be destroyed, which is expected to cause the valley Hall phase transition.

COMSOL Multiphysics was used to solve the dispersion relation of elastic-wave transport in periodic triangular lattices. Figure 2a shows the dispersion curve when the inter-coupling and intra-coupling radii are the same ($R_1 = R_2 = 2$ mm). It is shown that a degeneracy appears at point K in the dispersion relation. When the inter-coupling and intro-coupling radii are different ($R_1 = 3$ mm, $R_2 = 0.8$ mm), the dispersion relation curve is shown in Figure 2b, where the Dirac cone at point K is opened, and a bandgap is formed.

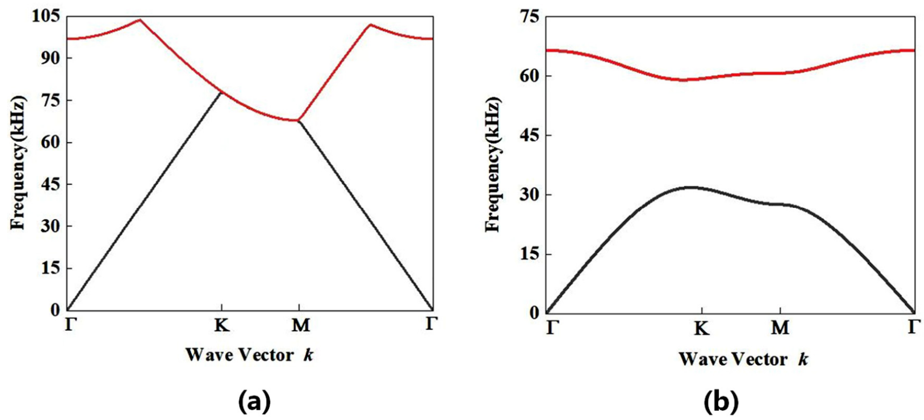

Figure 2. (**a**) Dispersion relation diagram for $R_1 = R_2 = 2$ mm (**b**) Dispersion relation diagram for $R_1 = 3$ mm, $R_2 = 0.8$ mm.

3. Valley Hall Effect Analogy

Figure 3a,b show the structure diagrams and dispersion curves for unit cells of type A and B, respectively. In Figure 3a, the intra-coupling radius (R_1) is larger than the inter-coupling (R_2) radius, which results a stronger intra-coupling compared with the inter-coupling. For the unit cell of type B shown in Figure 3b, the strengths of intra-coupling and inter-coupling inverse compared to type A. For each case, by breaking the space-inversion symmetry, a Dirac cone in two bands is opened and a complete band gap is formed.

The displacement fields of valley Modes 1–4 are calculated, as shown in Figure 3c. The results show that Mode 1 (the top valley of type-A unit cell) is obviously polarized (from left to right), while Mode 2 (the bottom valley of type-A unit cell) has no obvious polarization phenomenon, and the displacement is concentrated in the center of the unit cell. Similarly, for Mode 3 (the top valley of type-B unit cell), there is no obvious polarization phenomenon. In Mode 4 (the bottom valley of type-B unit cell), the displacement is significantly polarized to the left from right, and the displacement is concentrated in the center of the unit cell. It is shown that the polarization direction of type-A and type-B unit cells are opposite, indicating a chiral distribution. The existence of chiral polarization is an important feature of the valley mode. With these valley degrees of freedom, robust wave transports are expected to be achieved. It can be seen that the polarization direction reverses during the change from $R_1 > R_2$ to $R_1 < R_2$, and the topological phase is indeed transformed.

The influences of coupling-radii variations of the unit cell on the valley bandgap are further analyzed for the K point. Firstly, the inter-coupling radius in the unit cell is fixed as 2.5 mm and that of the intra-coupling radius is increased from 1 to 4 mm. In Figure 4a, it is shown that when $\Delta R \neq 0$, the bandgap opens up. The bandgap size increases with the increase of the absolute value of ΔR. In addition, the midgap frequency of the bands increases obviously with the increase of ΔR. Figure 4b shows the relationship between the bandgap value and ΔR. It can be seen that with the increase of the absolute value of ΔR, the bandgap value increases nonlinearly. Then, the intra-coupling radius in the unit cell is fixed as 2.5 mm and that of the inter-coupling radius is increased from 1 to 4 mm. Figure 4c,d shown that a similar conclusion can be obtained. Based on the above results, the required frequency band-structure can be achieved by selecting suitable coupling radii, which determine the frequency range of topological edge states.

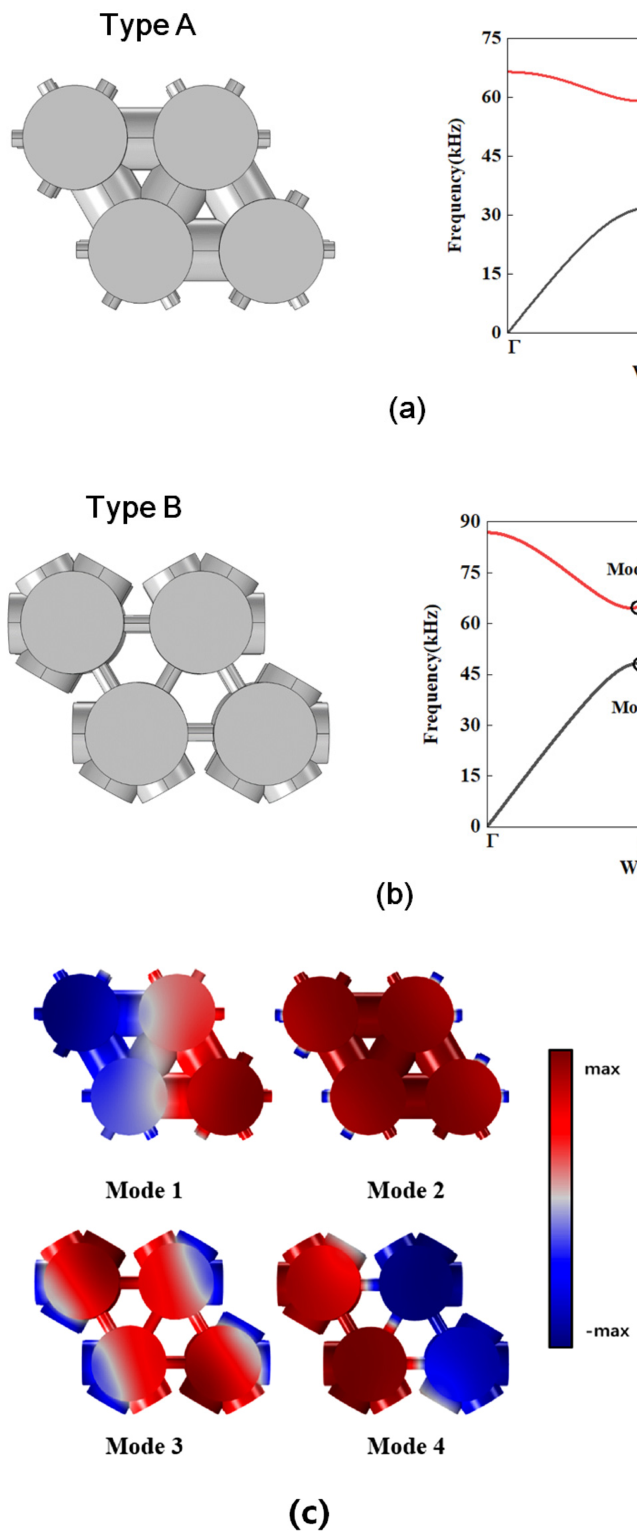

Figure 3. (**a**) The unit cell of type A and the according valley modes; (**b**) The unit cell of type B and the according valley modes; (**c**) Displacement field distributions of the valley modes.

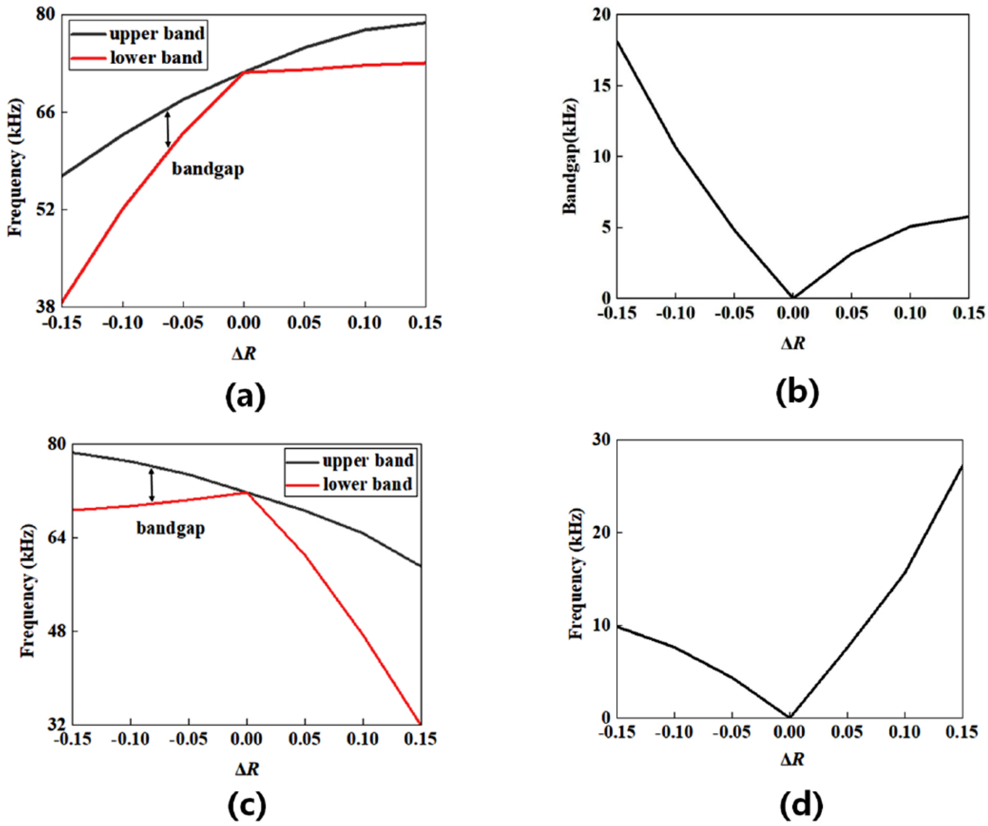

Figure 4. (**a**) Variation of frequency bands with ΔR ($R_2 = 2.5$ mm, $R_1 = 1$–4 mm) for K point; (**b**) Variation of bandgap value with ΔR ($R_2 = 2.5$ mm, $R_1 = 1$–4 mm); (**c**) Variation of frequency bands with ΔR ($R_1 = 2.5$ mm, $R_2 = 1$–4 mm); (**d**) Variation of bandgap value with ΔR ($R_1 = 2.5$ mm, $R_2 = 1$–4 mm).

4. Topological Valley Edge States

The topological phase transition is confirmed by the chiral polarization of displacement field distributions of the unit cells. In order to further verify the existence of topological edge states, a supercell is constructed. The unit cells of types A and B are jointed to form a supercell, making the periodicity in one direction of the structure disappear; namely, it degenerates into a finite structure in one direction, as shown in Figure 5a. The top and bottom boundaries along the y-direction are assigned free boundary conditions. The dispersion relations of the supercell are calculated, as shown in Figure 5b. The valley Hall edge states can be observed in the frequency range from 47 to 54 kHz, which are indicated by the line in the red dashed frame, and other lines correspond to bulk states. The displacement fields of the supercell for the edge-state frequency of 52 kHz are calculated, as shown in Figure 5c. It is shown that the domain wall can support edge states effectively.

In order to study the transport characteristics of elastic waves in the periodic triangular lattices, linear waveguides, Z-shaped waveguides and Z-shaped waveguides with defects are constructed. Figure 6a,c show the linear and Z-shaped waveguides, respectively. The structure consists of 12 × 12 unit cells. Periodic triangular lattices of types A and B are distributed in two sides of the path. The simulations are carried out via COMSOL Multiphysics. A wave source is set at the entrance of the waveguide. During FEM simulations, an absorbing boundary condition is applied to four outer edges of the structure to prevent wave reflections from the boundaries. The Solid Mechanics Module is used to model the lattice structure, a frequency-domain analysis is conducted to simulate the elastic-wave transport. The frequency range of scanning for the simulation is 40–60 kHz.

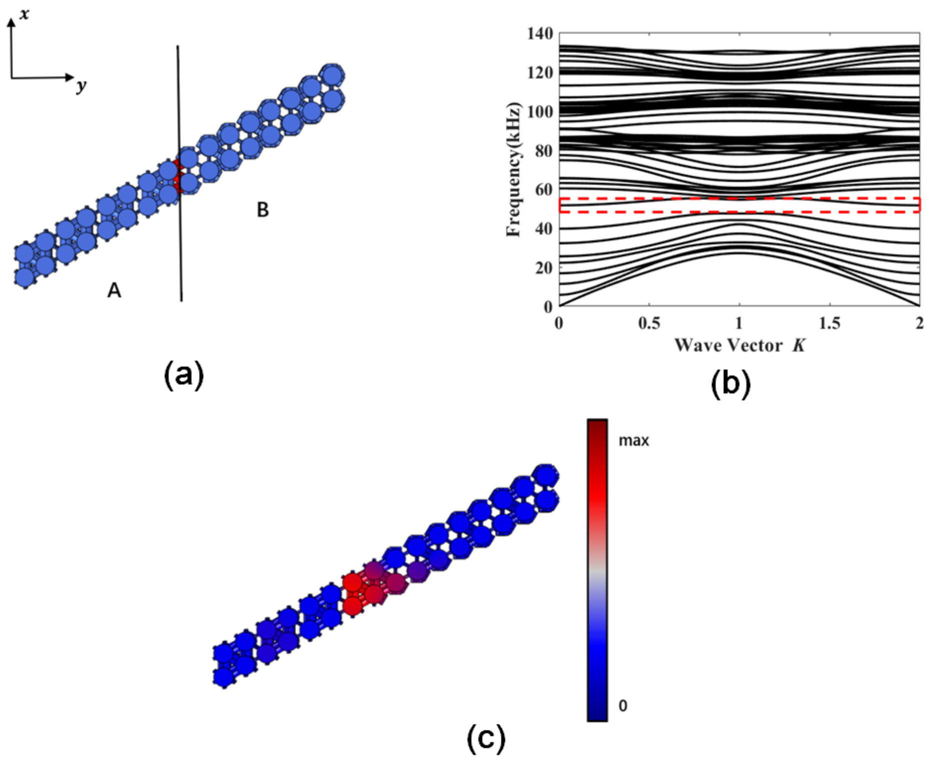

Figure 5. (**a**) Diagram of the supercell structure. (**b**) Dispersion curve of the supercell. (**c**) Displacement fields of the supercell.

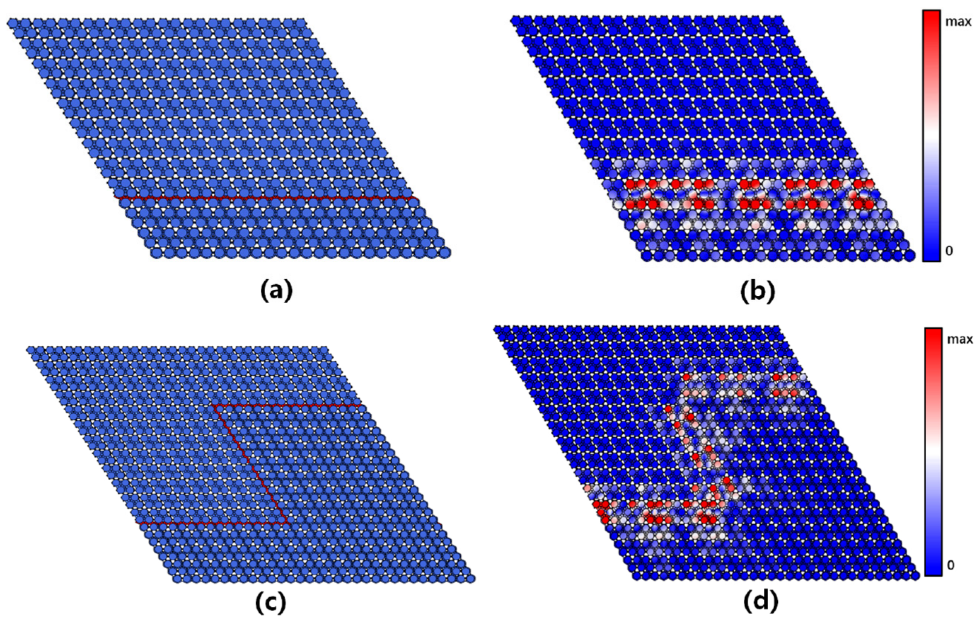

Figure 6. (**a**) Schematic diagram of the linear waveguide; (**b**) Topological transport of elastic waves in the linear waveguide; (**c**) Schematic diagram of the Z-shaped waveguide; (**d**) Topological transport of elastic waves in the Z-shaped waveguide.

The result of the wave transport in the linear waveguide is shown in Figure 6b. It can be found that the vibrations generated by the wave source can propagate along the path, and the energy is mainly concentrated on the interface and the scattering is not obvious. Figure 6d shows the result of the wave transport in the Z-shaped waveguide. Even if there are bending corners in the waveguide path, the backscattering is minor and the energy loss in propagation is very small.

In order to further verify the immunity of topological insulators to defects, a 16 × 16 Z-shaped waveguide with a defect is designed, shown in Figure 7a. An inter-coupling pillar in the path is deleted, forming a defect. The local magnification of the defect is shown in the right part of Figure 7a. The result of the wave transport is shown in Figure 7b. The existence of the defect does not obviously affect the wave transport. It is indicated that the topological insulator has a good immunity to the defect. On the interface composed of valley hall insulators with unit cells of types A and B, the valley phases on both sides of the interface are opposite, and the topological boundary states are formed. Therefore, elastic waves can propagate stably along the interface and are robust to defects and corners.

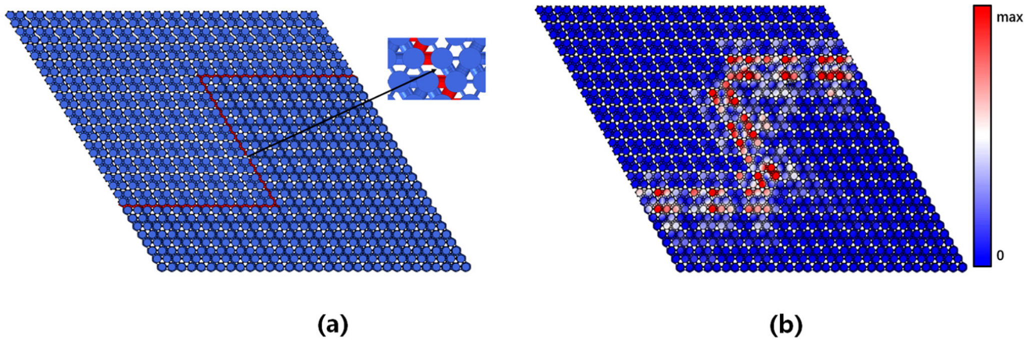

Figure 7. (**a**) Schematic diagram of a Z-shaped waveguide with a defect (an inter-coupling pillar is deleted); (**b**) Topological transport of elastic waves in the Z-shaped waveguide with a defect.

In addition, a direction-selective elastic energy splitter is designed based on the periodic triangular-lattice structure, as shown in Figure 8a. This splitter includes four sections consisted of lattices with unit-cell types A or B. Four interface paths are formed, which are labeled by OT, OU, OV and OW, respectively. To characterize the cross-waveguide splitter, a full-field numerical simulation of elastic-wave transports is performed, and the material and dimension parameters used are same to those in Section 3. The exciting positions are set in points U, V and W, respectively. The transport effects are shown in Figure 8b–d, respectively.

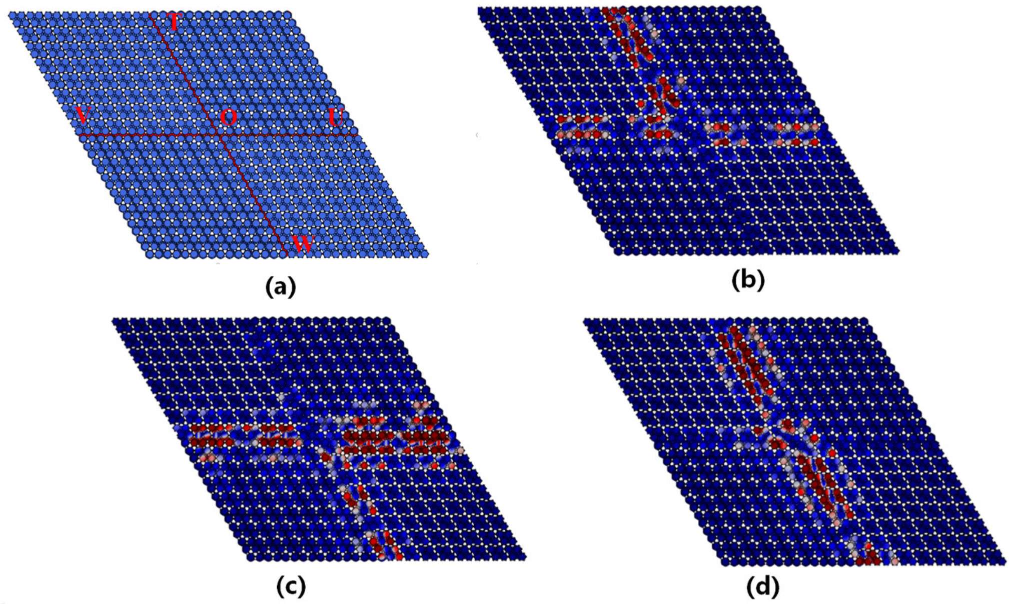

Figure 8. Direction-selective elastic energy splitter: (**a**) Schematic diagram of the elastic energy splitter; (**b**) Transport effect when the exciting point is set in T; (**c**) Transport effect when the exciting point is set in W; (**d**) Transport effect when the exciting point is set in O.

In Figure 8b, it can be seen that when the elastic wave is excited in Point T, the wave prefers to split and propagate back along OU and OV, eventually localizing at the left edge of the lattice without reaching the opposite edge (OW). Opposite group velocities between OT and OW interfaces result in elastic waves that cannot propagate straight through the junction. Figure 8c shows the result when the exciting point is selected in point W. Similarly, the elastic waves split and propagate back along OU and OV without reaching the opposite edge (OT). In addition, the exciting point is set in O, the effect of wave transport is shown in Figure 8d. It can be seen that the elastic wave split to only paths OU and OV. When the wave starts from point O, for paths OT and OW, the left is of lattice-type B and the right is of lattice-type A, which correspond to the interface mode in Section 3. For paths OU and OV, when the wave starts from point O, the left is of lattice-type A and the right is of lattice-type B, thus opposite group velocities are obtained. Therefore, the wave cannot propagate in the paths OU and OV.

5. Conclusions

In this paper, by utilizing the valley Hall effect obtained by breaking the spatial inversion symmetry of periodic triangular-lattice structures, the elastic wave topological valley transport is explored. It is shown that differences in intra-coupling and inter-coupling radii can cause the destruction of the effective spatial inversion symmetry, which gives rise to the forming of topological edge states. The valley bandgap width increases with larger differences between the two coupling radii. Topological transports of elastic waves traveling along linear and Z-shaped waveguides are realized with low scattering and immunity to defects. On this basis, a direction-selective elastic energy splitter based on the periodic triangular-lattice structure is obtained. The results presented in this work have good application prospects in elastic functional devices with arbitrary paths.

Author Contributions: Conceptualization, S.L., Z.T. and J.X.; methodology, Z.T. and I.K.; validation, S.L., Z.T. and T.M.; formal analysis, Z.T. and S.L.; investigation, S.L., Z.T. and F.S.; data curation, B.S., P.K., I.K. and I.N.; writing—original draft preparation, S.L., Z.T., B.W. and F.S.; writing—review and editing, T.M., I.K. and I.N.; supervision, Z.T. and T.M. All authors have read and agreed to the published version of the manuscript.

Funding: This work was supported by the National Natural Science Foundation of China (Nos. 12172183, 11772163), the Natural Science Foundation of Zhejiang Province (No. LY21A020007), One Health Interdisciplinary Research Project, Ningbo University. Prof. Iren Kuznetsova and Dr. Ilya Nedospasov thank to Russian Ministry of Science and Higher Education for financial support (agreement # 13.1902.21.0010).

Data Availability Statement: The data that support the findings of this study are available from the corresponding author upon reasonable request.

Conflicts of Interest: The authors declare no conflict of interest.

References

1. He, H.; Qiu, C.; Ye, L.; Cai, X.; Fan, X.; Ke, M.; Zhang, F.; Liu, Z. Topological negative refraction of surface acoustic waves in a Weyl phononic crystal. *Nature* **2018**, *560*, 61–64. [CrossRef] [PubMed]
2. Ji, C.Y.; Zhang, Y.; Liao, Y.; Zhou, X.; Jiang, J.H.; Zou, B.; Yao, Y. Fragile topologically protected perfect reflection for acoustic waves. *Phys. Rev. Res.* **2020**, *2*, 013131. [CrossRef]
3. Huber, S.D. Topological mechanics. *Nat. Phys.* **2016**, *12*, 621–623. [CrossRef]
4. Ge, H.; Yang, M.; Ma, C.; Lu, M.H.; Chen, Y.F.; Fang, N.; Sheng, P. Breaking the barriers: Advances in acoustic functional materials. *Natl. Sci. Rev.* **2018**, *5*, 159–182. [CrossRef]
5. Smirnov, A.; Anisimkin, V.; Voronova, N.; Shamsutdinova, E.; Li, P.; Ezzin, H.; Qian, Z.; Ma, T.; Kuznetsova, I. Multimode design and piezoelectric substrate anisotropy use to improve performance of acoustic liquid sensors. *Sensors* **2022**, *22*, 7231. [CrossRef] [PubMed]
6. Chen, M.; Meng, D.; Zhang, H.; Jiang, H.; Wang, Y. Resonance-coupling effect on broad band gap formation in locally resonant sonic metamaterials. *Wave Motion* **2016**, *63*, 111–119. [CrossRef]
7. Chen, M.; Jiang, H.; Zhang, H.; Li, D.; Wang, Y. Design of an acoustic superlens using single-phase metamaterials with a star-shaped lattice structure. *Sci. Rep.* **2018**, *8*, 1861. [CrossRef]

8. Yan, M.; Lu, J.; Li, F.; Deng, W.; Huang, X.; Ma, J.; Liu, Z. On-chip valley topological materials for elastic wave manipulation. *Nat. Mater.* **2018**, *17*, 993–998. [CrossRef]
9. Miniaci, M.; Pal, R.K.; Manna, R.; Ruzzene, M. Valley based splitting of topologically protected helical waves in elastic plates. *Phys. Rev. B* **2019**, *100*, 024304. [CrossRef]
10. Li, P.; Qian, Z.; Wang, B.; Kuznetsova, I.E.; Kolesov, V. The flexural-wave-based lens design for energy focusing via the trajectory prediction and the phase modulation. *Energy* **2021**, *220*, 119716. [CrossRef]
11. Gao, N.; Qu, S.; Si, L.; Wang, J.; Chen, W. Broadband topological valley transport of elastic wave in reconfigurable phononic crystal plate. *Appl. Phys. Lett.* **2021**, *118*, 063502. [CrossRef]
12. Swinteck, N.; Matsuo, S.; Runge, K.; Vasseur, J.O.; Lucas, P.; Deymier, P.A. Bulk elastic waves with unidirectional backscattering-immune topological states in a time-dependent superlattice. *J. Appl. Phys.* **2015**, *118*, 063103. [CrossRef]
13. Mousavi, S.H.; Khanikaev, A.B.; Wang, Z. Topologically protected elastic waves in phononic metamaterials. *Nat. Commun.* **2015**, *6*, 8682. [CrossRef] [PubMed]
14. Chen, H.; Zhang, H.; Wu, Q.; Huang, Y.; Nguyen, H.; Prodan, E.; Zhou, X.; Huang, G. Creating synthetic spaces for higher-order topological sound transport. *Nat. Commun.* **2021**, *12*, 5028. [CrossRef]
15. Huang, H.; Tan, Z.; Huo, S.; Feng, L.; Chen, J.; Han, X. Topologically protected zero refraction of elastic waves in pseudospin-Hall phononic crystals. *Commun. Phys.* **2020**, *3*, 46. [CrossRef]
16. Miniaci, M.; Pal, R.K.; Morvan, B.; Ruzzene, M. Experimental observation of topologically protected helical edge modes in patterned elastic plates. *Phys. Rev. X* **2018**, *8*, 031074. [CrossRef]
17. Wang, Z.; Li, H.; Liu, Z.; Luo, J.; Huang, F.; Huang, J.; Wang, X.; Li, H.; Yang, H. Probing two distinct types of topological rainbow concentrators related to the acoustic valley Hall insulator in synthesized three-dimensional space. *Phys. Rev. Appl.* **2022**, *17*, 064002. [CrossRef]
18. Rosa, M.I.N.; Pal, R.K.; Arruda, J.R.F.; Ruzzene, M. Edge states and topological pumping in spatially modulated elastic lattices. *Phys. Rev. Lett.* **2019**, *123*, 034301. [CrossRef]
19. Kane, C.L.; Lubensky, T.C. Topological boundary modes in isostatic lattices. *Nat. Phys.* **2014**, *10*, 39–45. [CrossRef]
20. Schaeffer, M.; Ruzzene, M. Wave propagation in reconfigurable magneto-elastic kagome lattice structures. *J. Appl. Phys.* **2015**, *117*, 194903. [CrossRef]
21. Wang, Z.; Wei, Q. An elastic higher-order topological insulator based on kagome phononic crystals. *J. Appl. Phys.* **2021**, *129*, 035102. [CrossRef]
22. Li, X.N.; Yu, S.Y.; Liu, H.; Lu, M.H.; Chen, Y.F. Topological mechanical metamaterials: A brief review. *Curr. Opin. Solid State Mater. Sci.* **2020**, *24*, 100853.